Progress In Electromagnetics Research, PIER 42, 303–337, 2003

ELECTROMAGNETIC HOLOGRAPHY ON CYLINDRICAL SURFACES USING K-SPACE TRANSFORMATIONS

M. A. Morgan

Department of Electrical and Computer Engineering
Naval Postgraduate School
Monterey, CA 93943, USA

Abstract—Spectral decomposition in 2-D k_z-m space is used to develop transfer functions that relate modal electromagnetic fields on concentric cylindrical surfaces. It is shown that all time-average radiated power is generated by superluminal modes (phase velocity $v_z > c$) which are confined to the baseband $|k_z| < k_0$. Subluminal modes, with k_z outside of the radiated band, are radially evanescent but permit recovery of imaging resolution that exceeds the usual diffraction limit provided by the radiated fields. Outward translation between cylinder surfaces is found to have a stable low-pass 2-D transfer characteristic in k_z-m space, where spatial resolution decreases with increased radius. The inverse transfer functions for inward translation of field components (termed backpropagation) employ a high-pass process that amplifies subluminal evanescent modes, thus potentially enhancing resolution while also amplifying measurement noise. A 2-D filter with flat elliptical passband and Gaussian roll-off is used to mitigate noise amplification with backpropagation. Outward translation and backpropagation are tested using sampled data on finite-length cylinders for various noise levels.

Acknowledgment

References

1. INTRODUCTION

In the design of efficient radiators or reduced cross-section platforms it is often necessary to perform measurements to spatially localize the radiated power sources on the test object. Although probes may be placed as close as desired to sample the field or current near to or on the object's surface, such invasive interrogation can perturb the surface fields or currents being sought. An alternative is to estimate near-surface quantities by back-propagating fields measured on a more distant surface where probe interaction with the test object is reduced. Such a procedure was applied by Ransom and Mittra [1] using plane wave expansions on parallel planes to locate defective elements in large phased arrays. Recent planar backpropagation to provide unobtrusive measurement of thin-films was reported by Harms, et al. [2]. Joy, et al. [3–5] developed microwave holography to estimate fields on a minimal spherical surface enclosing an antenna or radome by estimating spherical harmonics on a larger surface through sampled measurement of the tangential electric field. Medgyesi-Mitschang, et al. [6, 7] have investigated ultra near-fields for bodies of translation using ω-k representations. A finite-element solution was used by Wawrzyniak [8] to perform near-field holography of currents on metal surfaces of revolution.

Developments in acoustic imaging and radiation by Williams, et al. [9–12], uncovered the supersonic nature of cylindrical surface acoustic modes that provide outbound radiation. This mechanism can be exploited to enhance the backpropagation of field measurements by selectively mitigating effects of noise that accompany subsonic evanescent contributions. Use of near-field data provides the potential for enhanced resolution in imaging that exceeds the usual $\lambda/2$ diffraction limit associated with use of far-fields.

The k-space concept developed for acoustics has been reformulated for application to the vector electromagnetic field [13, 14]. This will be considered in the next section. After investigating the properties of superluminal and subluminal modes in Section 3, the transformations for cylindrical translation of the field components will be derived, displayed and discussed in Section 4. Results of computational tests will then be considered for both outward translation and backpropagation, with and without additive noise.

Figure 1 depicts the example source to be considered: an array

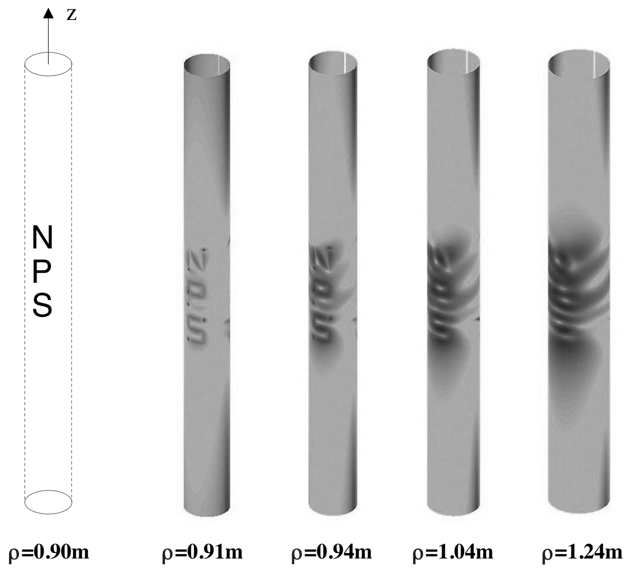

(a)

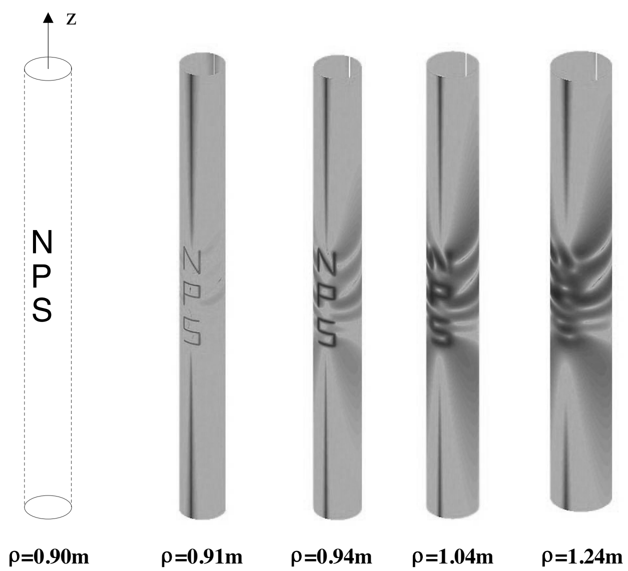

(b)

Figure 1. (a) $|\overline{E}_{tan}|$ and (b) $|\overline{H}_{tan}|$ on concentric cylinder surfaces due to wire source conformal to $\rho = 0.90\,\mathrm{m}$ cylinder.

composed of three thin-wire elements roughly in the shape of N, P and S. These wire elements conform to the surface of a geometrical cylinder having radius $\rho = 0.9\,\mathrm{m}$ and are each $1\,\mathrm{m}$ high with $0.5\,\mathrm{m}$ vertical spacing and subtend an azimuth angle of 45°. The wires are driven by a uniformly distributed 1A current with zero phase at $f = 300\,\mathrm{MHz}$ (with convenient $\lambda_0 = 1\,\mathrm{m}$). Using ultra-fine wire segmentation (segment length $< \lambda/500$) and exact integration formulas [15], highly accurate fields were computed on a suite of concentric cylinders of length $20\,\mathrm{m}$. Figure 1 shows examples of computed $|\overline{E}_{tan}|$ and $|\overline{H}_{tan}|$ on cylinders of increasing radii. Log-intensity plots are used, each with a local scale factor, to provide enhanced dynamic range.

The fields display the expected spatial "smearing" with increasing radius due to the R^{-n} weighted contributions in the Green's function integration. Fields very close to the source cylinder are most strongly produced by the nearby source segments while fields at larger radii embody a more global mixing of phased contributions from all wire segments. The resultant field smearing as radius increases is accompanied by a reduction of modal bandwidth in k_z-m space — essentially low-pass filtering. Outward translation should thus provide some degree of noise-tolerance. This behavior will be demonstrated.

Backpropagation to smaller radii produces an inverse effect, where inward translated fields (and any additive noise) are high-pass filtered in k_z-m space. Without compensation by low-pass filtering, the broadband noise or other inaccuracies in sampled fields are amplified enormously in attempting even a small (e.g., $\lambda/10$) inward translation. With proper 2-D low-pass filtering, as employed in the performance tests, it is possible to backpropagate the smeared field distributions on the largest cylinder in Figure 1 (adding noise) to produce more highly resolved fields akin to those on the smaller radius cylinders. The accuracy of such holographic resolution enhancement is dependent upon the relative 2-D k_z-m space bandwidths of the fields at the two radii involved and the signal to noise ratio (SNR) of the measured field. Sampled data with SNR as low as $20\,\mathrm{dB}$ and translations as great as 0.46λ will be considered in Section 4.

2. MODAL FIELD FORMULATION

Circular cylindrical coordinates (ρ, ϕ, z) as depicted in Figure 2 are employed with phasor fields using suppressed time-harmonic behavior $e^{\jmath\omega t}$. Fields will be represented outside of a cylindrical surface which encloses a finite size radiating source, such as an antenna or a scatterer. Material in the unbounded region external to the cylinder is assumed lossless, homogeneous and isotropic, with material constants $\epsilon(\omega)$ and

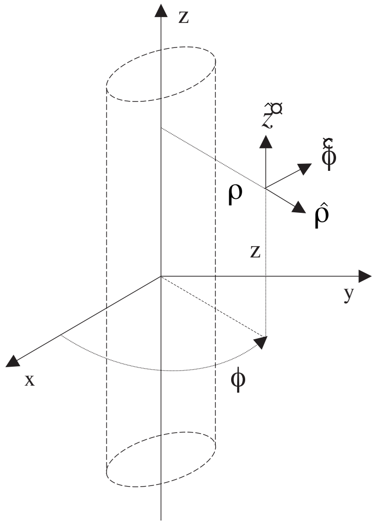

Figure 2. Cylindrical coordinates and unit vectors.

$\mu(\omega)$.

Radial translation will utilized fields decomposed into cylindrical modes. As with enclosed waveguides [16], modal fields can be categorized as transverse magnetic (TM) "E-waves" having $H_z = 0$ and transverse electric (TE) "H-waves" having $E_z = 0$.

Maxwell's source-free equations, $\nabla \times \overline{E} = -\jmath\omega\mu\overline{H}$ and $\nabla \times \overline{H} = \jmath\omega\epsilon\overline{E}$, with assumed $e^{-\jmath k_z z}$ traveling wave variation, can be manipulated to generate transverse fields, $\overline{E}_t = \overline{E}_t^{\mathrm{TM}} + \overline{E}_t^{\mathrm{TE}}$ and $\overline{H}_t = \overline{H}_t^{\mathrm{TM}} + \overline{H}_t^{\mathrm{TE}}$, using either E_z or H_z

$$\overline{E}_t^{\mathrm{TM}} = \frac{-\jmath k_z}{k_\rho^2}\nabla_2 \, E_z \tag{1a}$$

$$\overline{H}_t^{\mathrm{TM}} = \frac{-\jmath\omega\epsilon}{k_\rho^2}\hat{z}\times\nabla_2 \, E_z = \frac{\omega\epsilon}{k_z}\hat{z}\times\overline{E}_t^{\mathrm{TM}} \tag{1b}$$

$$\overline{H}_t^{\mathrm{TE}} = \frac{-\jmath k_z}{k_\rho^2}\nabla_2 \, H_z \tag{2a}$$

$$\overline{E}_t^{\mathrm{TE}} = \frac{\jmath\omega\mu}{k_\rho^2}\hat{z}\times\nabla_2 \, H_z = \frac{\omega\mu}{k_z}\overline{H}_t^{\mathrm{TE}}\times\hat{z} \tag{2b}$$

where $\nabla_2 = \frac{\partial}{\partial\rho}\hat{\rho} + \frac{1}{\rho}\frac{\partial}{\partial\phi}\hat{\phi}$ is the 2-D Laplacian operator defined in the transverse plane. The radial wavenumber is given by $k_\rho = \sqrt{k^2 - k_z^2}$, with $k = \omega\sqrt{\mu\epsilon} = \frac{\omega}{v_p}$, where v_p is the phase velocity of plane-wave propagation in the medium. Equations (1b) and (2b) imply that $\mathcal{Z}^{\mathrm{TM}} = \frac{k_z}{\omega\epsilon}$ and $\mathcal{Z}^{\mathrm{TE}} = \frac{\omega\mu}{k_z}$ are transverse field wave impedances.

Longitudinal fields satisfy the Helmholtz equation,

$$\left(\nabla^2 + k^2\right) E_z(\rho, \phi, z) = 0 \tag{3a}$$

$$\left(\nabla^2 + k^2\right) H_z(\rho, \phi, z) = 0 \tag{3b}$$

whose separation of variables product solution in cylindrical coordinates has the modal form $H_m^{(2)}(k_\rho\rho)\; e^{\jmath m\phi}\; e^{-\jmath k_z z}$. The Hankel function of the second kind, $H_m^{(2)}$, provides outbound radiation when using $e^{\jmath\omega t}$ time-convention.

Substituting modal E_z and H_z solutions having $e^{\jmath m\phi}\; e^{-\jmath k_z z}$ functional form into (1) and (2) yields transverse modal fields having the same (ϕ, z) behavior. Such separable modes each satisfy Maxwell's equations and form a Fourier basis for assembly of complete vector fields using

$$\overline{E}(\rho, \phi, z) = \sum_{m=-\infty}^{\infty} \overline{e}_m(\rho, z)\; e^{\jmath m\phi} \tag{4a}$$

$$\overline{H}(\rho, \phi, z) = \sum_{m=-\infty}^{\infty} \overline{h}_m(\rho, z)\; e^{\jmath m\phi} \tag{4b}$$

with azimuthal Fourier modes

$$\overline{e}_m(\rho, z) = \frac{1}{2\pi} \int_{-\infty}^{\infty} \overline{\mathcal{E}}_m(\rho, k_z)\; e^{-\jmath k_z z}\; dk_z \tag{5a}$$

$$\overline{h}_m(\rho, z) = \frac{1}{2\pi} \int_{-\infty}^{\infty} \overline{\mathcal{H}}_m(\rho, k_z)\; e^{-\jmath k_z z}\; dk_z \tag{5b}$$

The spectral vector functions, $\overline{\mathcal{E}}_m(\rho, k_z)$ or $\overline{\mathcal{H}}_m(\rho, k_z)$, are evaluated at a specific ρ using 2-D Fourier transforms of the phasor fields,

$$\overline{\mathcal{E}}_m(\rho, k_z) = \frac{1}{2\pi} \int_0^{2\pi} \int_{-\infty}^{\infty} \overline{E}(\rho, \phi, z)\; e^{-\jmath m\phi}\; e^{\jmath k_z z}\; dz\; d\phi \tag{6a}$$

$$\overline{\mathcal{H}}_m(\rho, k_z) = \frac{1}{2\pi} \int_0^{2\pi} \int_{-\infty}^{\infty} \overline{H}(\rho, \phi, z)\; e^{-\jmath m\phi}\; e^{\jmath k_z z}\; dz\; d\phi \tag{6b}$$

The form for the longitudinal spectral components is found using the separation of variables product solution to (3),

$$\mathcal{E}_{z,m}(\rho, k_z) = a_m(k_z)\; H_m^{(2)}(k_\rho\rho) \quad \text{TM Case} \tag{7a}$$

$$\mathcal{H}_{z,m}(\rho, k_z) = b_m(k_z)\; H_m^{(2)}(k_\rho\rho) \quad \text{TE Case} \tag{7b}$$

Note the radial invariance of $a_m(k_z)$ and $b_m(k_z)$. This forms the basis for translating fields between cylindrical surfaces.

Substituting (4) and (5) into (1) and (2) with use of (7), provides explicit generating equations for the TM and TE portions of the transverse field, resulting in,

$$\begin{aligned}\mathcal{E}_{\rho,m}(\rho,k_z) &= \frac{-\jmath k_z}{k_\rho^2}\,\frac{\partial}{\partial\rho}\mathcal{E}_{z,m}(\rho,k_z) + \frac{m\omega\mu}{k_\rho^2\,\rho}\,\mathcal{H}_{z,m}(\rho,k_z)\\ &= -k_z\,G_m(\rho,k_z)\,a_m(k_z) + \omega\mu\,F_m(\rho,k_z)\,b_m(k_z) \qquad \text{(8a)}\\ \mathcal{E}_{\phi,m}(\rho,k_z) &= \frac{m\,k_z}{k_\rho^2\,\rho}\,\mathcal{E}_{z,m}(\rho,k_z) + \frac{\jmath\omega\mu}{k_\rho^2}\,\frac{\partial}{\partial\rho}\,\mathcal{H}_{z,m}(\rho,k_z)\\ &= k_z F_m(\rho,k_z)\,a_m(k_z) + \omega\mu\,G_m(\rho,k_z)\,b_m(k_z) \qquad \text{(8b)}\\ \mathcal{H}_{\rho,m}(\rho,k_z) &= \frac{-m\omega\epsilon}{k_\rho^2\,\rho}\,\mathcal{E}_{z,m}(\rho,k_z) - \frac{\jmath k_z}{k_\rho^2}\,\frac{\partial}{\partial\rho}\mathcal{H}_{z,m}(\rho,k_z)\\ &= -\omega\epsilon\,F_m(\rho,k_z)\,a_m(k_z) - k_z\,G_m(\rho,k_z)\,b_m(k_z) \qquad \text{(8c)}\\ \mathcal{H}_{\phi,m}(\rho,k_z) &= \frac{-\jmath\omega\epsilon}{k_\rho^2}\,\frac{\partial}{\partial\rho}\,\mathcal{E}_{z,m}(\rho,k_z) + \frac{m\,k_z}{k_\rho^2\,\rho}\,\mathcal{H}_{z,m}(\rho,k_z)\\ &= -\omega\epsilon\,G_m(\rho,k_z)\,a_m(k_z) + k_z\,F_m(\rho,k_z)\,b_m(k_z) \qquad \text{(8d)}\end{aligned}$$

where

$$F_m(\rho,k_z) = \frac{m}{k_\rho^2\,\rho}\,H_m^{(2)}(k_\rho\rho) \qquad \text{(9a)}$$

$$G_m(\rho,k_z) = \frac{\jmath}{k_\rho}\,H_m^{(2)\,\prime}(k_\rho\rho) \qquad \text{(9b)}$$

3. RADIATION AND EVANESCENCE

As a prelude to development of the field translation procedure, it is important to understand the spectral behavior of Fourier modes relative to cylindrical radius in the context of radiation, evanescence and power flow. Consider first the case of a lossless circular metallic waveguide, where TM and TE modal fields are represented using a positive real k_ρ spectrum. Enforcement of $E_z = E_\phi = 0$ at the conductor radius constrains k_ρ to discrete, quantized modal indices. Propagating field modes that convey time-average power in the waveguide have real $k_z = \sqrt{k^2 - k_\rho^2}$ only for $k_\rho < k$. Power is thus conveyed with real k_z between $\pm k$. Cutoff modes have $k_\rho > k$, with associated imaginary k_z. These correspond to evanescent fields that attenuate with $\pm z$ and carry no time-average power.

In contrast, the modal fields in the unbounded region being considered will have a continuous real k_z spectrum. Fields propagate and convey power in the $\pm z$ direction for all real k_z. When $k_z < k$, the associated real k_ρ provides radial field propagation and outward power flow. The k_ρ becomes imaginary for $k_z > k$, resulting in radial evanescence and cutoff of outbound power flow. This will be demonstrated.

As in the case of waveguides, longitudinal phase and group velocities can be defined respectively as $v_z = \frac{\omega}{k_z}$ and $v_g = \frac{d\omega}{dk_z}$ for modes in the unbounded external region [17]. The phase velocity can exceed that of a plane wave in the medium,

$$|v_z| = \frac{\omega}{|k_z|} > \frac{\omega}{k} = v_p \quad \text{when } |k_z| < k \tag{10}$$

The corresponding spectral region $|k_z| < k$ is termed "superluminal." Likewise, $|k_z| > k$ is denoted as the "subluminal" portion of the spectrum since $v_z < v_p$. In an air-filled waveguide, for example, only superluminal modes propagate, each with phase velocity exceeding that of light. This does not violate Einstein's postulate that transport velocities never exceed c since modal energy and modulated information travel down the guide at the group velocity [17], where $v_g < c$.

Radial evanescence of subluminal fields can be observed for $\mathcal{E}_{z,m}$ and $\mathcal{H}_{z,m}$ as they appear in (7) by denoting $k_\rho = \sqrt{k^2 - k_z^2} = -\jmath\sqrt{k_z^2 - k^2} = -\jmath\alpha$ and expressing the Hankel functions [18] as

$$H_m^{(2)}(-\jmath\alpha\rho) = \frac{2}{\pi}\,\jmath^{m+1}\,K_m(\alpha\rho) \tag{11}$$

for imaginary argument when $|k_z| > k$. The modified Bessel functions of the second kind, $K_m(\alpha\rho)$, provide accelerated radial decay with large argument amplitude proportional to $e^{-\alpha\rho}/\sqrt{\alpha\rho}$.

Within the $|k_z| < k$ superluminal band, k_ρ remains real and $H_m^{(2)}(k_\rho\rho)$ has slowly decaying outward traveling wave behavior, with large argument amplitude proportional to $1/\sqrt{k_\rho\rho}$. As will now be shown, all outbound time-average power is generated by the superluminal portion of the spectrum.

Power passing through an infinite length cylindrical surface of radius ρ can be expressed by surface integration of the radially directed time-average Poynting vector, $P_\rho = \frac{1}{2}\mathrm{Re}\{(\overline{E}\times\overline{H}^*)\cdot\hat{\rho}\}$ where * indicates conjugation. Expressing P_ρ in terms of field components tangential to the cylindrical integration surface gives

$$W=\int_{-\infty}^{\infty}\int_{0}^{2\pi}\frac{1}{2}\mathrm{Re}\{-E_z(\rho,\phi,z)H_\phi^*(\rho,\phi,z)+E_\phi(\rho,\phi,z)H_z^*(\rho,\phi,z)\}\rho d\phi dz \tag{12}$$

Power conservation requires that W is independent of ρ for lossless media.

Substitution of (4) into (12), with integration of exponential cross terms on ϕ gives

$$W = \sum_{m=-\infty}^{\infty} \int_{-\infty}^{\infty} p_m(\rho, z)\, dz = \sum_{m=-\infty}^{\infty} \int_{-\infty}^{\infty} \mathcal{P}_m(k_z)\, dk_z \tag{13}$$

with modal radiated power density per unit length,

$$p_m(\rho, z) = \pi\rho\, \mathrm{Re}\{-e_{z,m}(\rho, z)\; h_{\phi,m}^*(\rho, z) + e_{\phi,m}(\rho, z)\; h_{z,m}^*(\rho, z)\} \tag{14}$$

Noting the definitions in (5), the generalized Parseval's formula [19] equating integral products of functions and their Fourier transforms, is used to define the power spectral density (PSD) in k_z on the right-hand side of (13),

$$\mathcal{P}_m(k_z) = \frac{\rho}{2}\, \mathrm{Re}\{-\mathcal{E}_{z,m}(\rho, k_z)\; \mathcal{H}_{\phi,m}^*(\rho, k_z) + \mathcal{E}_{\phi,m}(\rho, k_z)\; \mathcal{H}_{z,m}^*(\rho, k_z)\} \tag{15}$$

Note the explicit omission of radial dependence in the PSD. This can be demonstrated by substituting field components in (7), (8) and (9) into (15). The term involving products of $a_m(k_z)$ and $b_m(k_z)$ is found to be zero, leaving distinct TM and TE contributions,

$$\mathcal{P}_m(k_z) = \mathcal{P}_m^{\mathrm{TM}}(k_z) + \mathcal{P}_m^{\mathrm{TE}}(k_z) \tag{16a}$$

where

$$\mathcal{P}_m^{\mathrm{TM}}(k_z) = \frac{\omega\epsilon\rho\; |a_m(k_z)|^2}{2}\, \mathrm{Re}\{-\jmath H_m^{(2)}(k_\rho\rho)\; [H_m^{(2)\,\prime}(k_\rho\rho)]^*/k_\rho\} \tag{16b}$$

$$\mathcal{P}_m^{\mathrm{TE}}(k_z) = \frac{\omega\mu\rho\; |b_m(k_z)|^2}{2}\, \mathrm{Re}\{\jmath H_m^{(2)\,\prime}(k_\rho\rho)\; [H_m^{(2)}(k_\rho\rho)]^*/k_\rho\} \tag{16c}$$

Consider specializing (16) to superluminal and subluminal cases. For superluminal modes, having real k_ρ, first substitute $H_m^{(2)}(k_\rho\rho) = J_m(k_\rho\rho) - \jmath N_m(k_\rho\rho)$ into (16), where J_m and N_m are respective Bessel and Neumann functions. Use of the Wronskian [18],

$J_m(k_\rho\rho)\ N_m^{'}(k_\rho\rho) - J_m^{'}(k_\rho\rho)\ N_m(k_\rho\rho) = \dfrac{2}{\pi k_\rho \rho}$, yields the simplified result,

$$\mathcal{P}_m(k_z) = \frac{\omega}{\pi\ (k^2 - k_z^2)} \left[\epsilon\ |a_m(k_z)|^2 + \mu\ |b_m(k_z)|^2\right] \tag{17}$$

valid for the superluminal range $|k_z| < k$. As expected, the result is not a function of ρ.

Now consider the subluminal region, where $k_\rho = -\jmath\alpha = -\jmath\sqrt{k_z^2 - k^2}$. Substituting (11) into (16) gives

$$\mathcal{P}_m(k_z) = \frac{2\omega\rho}{\alpha\pi^2} \left[\epsilon\ |a_m(k_z)|^2 + \mu|b_m(k_z)|^2\right] \mathrm{Re}\{-\jmath K_m(\alpha\rho) K_m^{'}(\alpha\rho)\} = 0 \tag{18}$$

thus showing that outbound time-average power is generated only by field modes in the $|k_z| < k$ superluminal band.

4. RADIAL TRANSLATION OF FIELDS

Field translation is seemingly straightforward using the radial invariance of $a_m(k_z)$ and $b_m(k_z)$ as defined in (7). These coefficients may be theoretically computed from the Fourier transforms in (6) using $E_z(\rho_1, \phi, z)$ and $H_z(\rho_1, \phi, z)$ on an infinite length cylindrical surface of radius, ρ_1. Field components of the k_z-m spectra can then be constructed, in principle, at any radius, ρ_2, by use of equations (7) and (8). Inverting these spectra via (4) and (5) yields the radially translated components of $\overline{E}(\rho_2, \phi, z)$ and $\overline{H}(\rho_2, \phi, z)$.

Implementation of this technique to sampled data on finite-length cylinders requires replacement of continuous function Fourier transforms and series with discrete transforms computed using FFT's in z and ϕ. Errors will result even with perfect noise-free sampled field data due to aliasing of spectral contributions having spatial frequencies that exceed one-half of the sampling rates in z or the metrical distance $(\rho\ \phi)$. Use of discrete Fourier series in k_z with the truncated cylinder introduces a virtual periodic extension of the truncated cylinder source fields at ρ_1.

Even with aliasing and truncation errors in $a_m(k_z)$ and $b_m(k_z)$, it is possible to recover outward translated fields at $\rho_2 > \rho_1$ using (7) and (8) since the process tends to de-emphasize higher order coefficients through low-pass filtering. As shown in the previous section, for sufficiently large ρ (typically greater than about λ from the source) only radiation fields remain, with spectal content $|k_z| < k$.

Backpropagation using $a_m(k_z)$ and $b_m(k_z)$ was found to be viable for estimating E_z and H_z, via (7), if proper low-pass filtering is used to compensate for high-pass amplification of errors in higher order computed coefficients. The other field components could not be successfully reconstructed using this approach when $\rho_2 < \rho_1$, even in the noise-free case. The reason for this failure appears to be the additional error provided by the derivatives required in (8).

A better route is to define operators that directly translate like pairs of spectral field components between ρ_1 and ρ_2. For example, the use of a_m and b_m radial invariance in (7) gives

$$\begin{bmatrix} \mathcal{E}_{z,m}(\rho_2, k_z) \\ \mathcal{H}_{z,m}(\rho_2, k_z) \end{bmatrix} = T_m(\rho_1, \rho_2, k_z) \begin{bmatrix} \mathcal{E}_{z,m}(\rho_1, k_z) \\ \mathcal{H}_{z,m}(\rho_1, k_z) \end{bmatrix} \tag{19a}$$

with scalar translation operator

$$T_m(\rho_1, \rho_2, k_z) = \frac{H_m^{(2)}(k_\rho \rho_2)}{H_m^{(2)}(k_\rho \rho_1)} \tag{19b}$$

Translation of transverse field spectra involves pairwise solutions of equations in (8) with assumed ρ-independent $a_m(k_z)$ and $b_m(k_z)$. For example, (8b) and (8d) can be combined to yield

$$\begin{bmatrix} \mathcal{E}_{\phi,m}(\rho, k_z) \\ \mathcal{H}_{\phi,m}(\rho, k_z) \end{bmatrix} = [V_m(\rho_2, k_z)] \cdot \begin{bmatrix} a_m(k_z) \\ b_m(k_z) \end{bmatrix} \tag{20a}$$

with array operator constructed from functions defined in (9),

$$[V_m(\rho, k_z)] = \begin{bmatrix} k_z\, F_m(\rho, k_z) & \omega\mu\, G_m(\rho, k_z) \\ -\omega\epsilon\, G_m(\rho, k_z) & k_z\, F_m(\rho, k_z) \end{bmatrix} \tag{20b}$$

Inverting (20a) at ρ_1 then using the resulting a_m and b_m to drive (20a) at ρ_2 provides azimuthal component translation via

$$\begin{bmatrix} \mathcal{E}_{\phi,m}(\rho_2, k_z) \\ \mathcal{H}_{\phi,m}(\rho_2, k_z) \end{bmatrix} = [V_m(\rho_2, k_z)] \cdot [V_m(\rho_1, k_z)]^{-1} \cdot \begin{bmatrix} \mathcal{E}_{\phi,m}(\rho_1, k_z) \\ \mathcal{H}_{\phi,m}(\rho_1, k_z) \end{bmatrix} \tag{20c}$$

Translation of radial field components is formulated by a similar procedure using (8a) and (8c),

$$\begin{bmatrix} \mathcal{E}_{\rho,m}(\rho_2, k_z) \\ \mathcal{H}_{\rho,m}(\rho_2, k_z) \end{bmatrix} = [U_m(\rho_2, k_z)] \cdot [U_m(\rho_1, k_z)]^{-1} \cdot \begin{bmatrix} \mathcal{E}_{\rho,m}(\rho_1, k_z) \\ \mathcal{H}_{\rho,m}(\rho_1, k_z) \end{bmatrix} \tag{21a}$$

where,

$$[U_m(\rho, k_z)] = \begin{bmatrix} -k_z\ G_m(\rho, k_z) & \omega\mu\ F_m(\rho, k_z) \\ -\omega\epsilon\ F_m(\rho, k_z) & -k_z\ G_m(\rho, k_z) \end{bmatrix} \tag{21b}$$

The matrix product in (20c) can be evaluated to give

$$\begin{bmatrix} \mathcal{E}_{\phi,m}(\rho_2, k_z) \\ \mathcal{H}_{\phi,m}(\rho_2, k_z) \end{bmatrix} = \begin{bmatrix} S1_m(\rho_1, \rho_2, k_z) & \jmath\omega\mu S2_m(\rho_1, \rho_2, k_z) \\ -\jmath\omega\epsilon S2_m(\rho_1, \rho_2, k_z) & S1_m(\rho_1, \rho_2, k_z) \end{bmatrix} \begin{bmatrix} \mathcal{E}_{\phi,m}(\rho_1, k_z) \\ \mathcal{H}_{\phi,m}(\rho_1, k_z) \end{bmatrix} \tag{22a}$$

where

$$S1_m(\rho_1, \rho_2, k_z) = \frac{m^2\ k_z^2(\frac{\rho_1}{\rho_2})H_m^{(2)}(k_\rho\rho_2) - k^2k_\rho^2\rho_1^2 H_m^{(2)'}(k_\rho\rho_2)D_m(k_\rho\rho_1)}{m^2k_z^2H_m^{(2)}(k_\rho\rho_1) - k^2k_\rho^2\rho_1^2H_m^{(2)'}(k_\rho\rho_1)D_m(k_\rho\rho_1)} \tag{22b}$$

and

$$S2_m(\rho_1, \rho_2, k_z) = \frac{mk_zk_\rho\rho_1\left\{H_m^{(2)'}(k_\rho\rho_2) - (\frac{\rho_1}{\rho_2})H_m^{(2)}(k_\rho\rho_2)D_m(k_\rho\rho_1)\right\}}{m^2k_z^2H_m^{(2)}(k_\rho\rho_1) - k^2k_\rho^2\rho_1^2H_m^{(2)'}(k_\rho\rho_1)D_m(k_\rho\rho_1)} \tag{22c}$$

with

$$D_m(k_\rho\rho_1) = \frac{H_m^{(2)'}(k_\rho\rho_1)}{H_m^{(2)}(k_\rho\rho_1)} \tag{22d}$$

These translation operators provide low-pass filtering for robust outward translation with $\rho_2 > \rho_1$. On the other hand, when $\rho_2 < \rho_1$, they generate high-pass filtering and unacceptable error amplification even without additive noise. This dual behavior can be explained by recalling that in outbound propagation the PSD for time-average radiated power, $\mathcal{P}_m(k_z)$, is confined to the superluminal band $|k_z| < k$ and is independent of ρ, per (17). Close to the source, superluminal modal fields exhibit slow radial decay, phase rotation and dispersive mixing associated with near-field radiation. In the subluminal region $|k_z| > k$, where $\mathcal{P}_m(k_z) = 0$, modal fields are strictly evanescent. This is expressed as the rapid radial decay of modified Bessel functions,

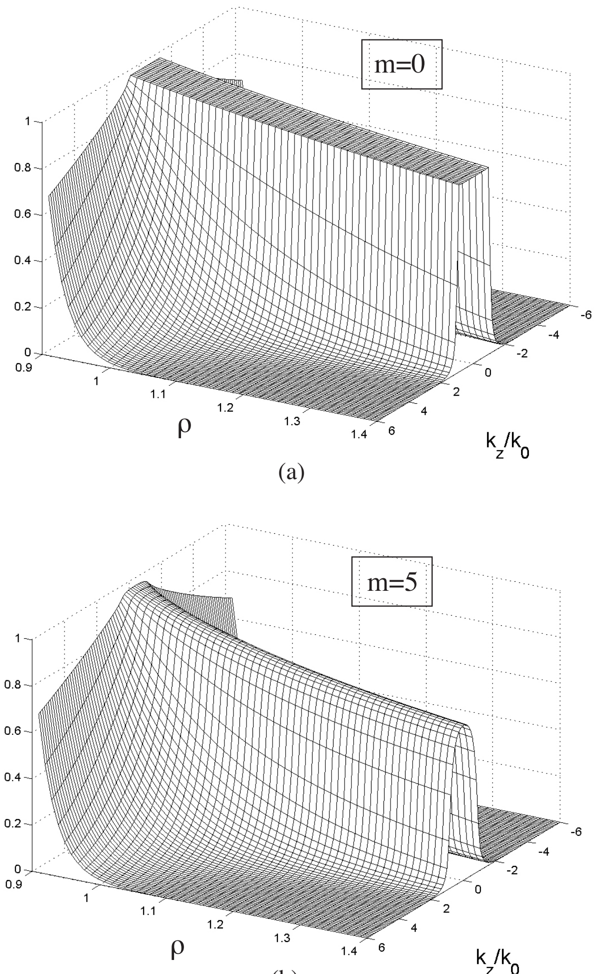

(a)

(b)

Figure 3. $|T_m(\rho_1, \rho_2, k_z)|$: Outward translation from $\rho_1 = 0.90\,\mathrm{m} \to \rho_2 = 0.91\,\mathrm{m}$ to $1.4\,\mathrm{m}$. (a) $m = 0$ and (b) $m = 5$.

$K_m(\alpha\rho)$. The effective k_z bandwidth for the modal fields thus collapses rapidly with increasing ρ about the superluminal radiation passband between $\pm k$.

The low-pass filtering effect for outward translation is illustrated in Figure 3 for $T_m(\rho_1, \rho_2, k_z)$ with $m = 0$ and $m = 5$. Fixing $\rho_1 = 0.9\lambda$, the k_z spectrum magnitude is plotted for ρ_2 ranging from 0.91λ to 1.4λ. Figure 4 displays backpropagation induced high-pass filtering

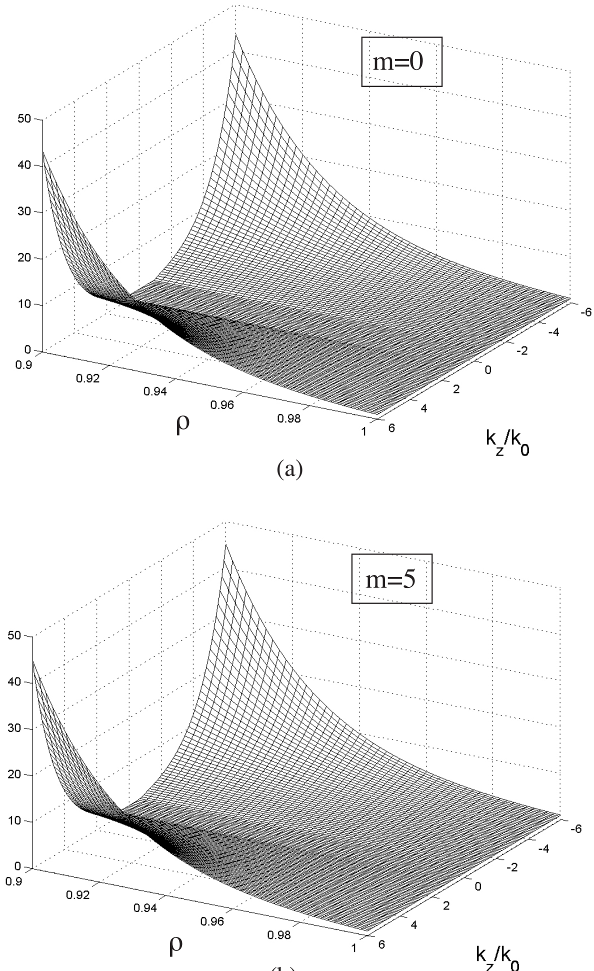

(a)

(b)

Figure 4. $|T_m(\rho_1, \rho_2, k_z)|$: Backpropagation from $\rho_1 = 1.0\,\mathrm{m} \rightarrow \rho_2 = 0.90\,\mathrm{m}$ to $1.0\,\mathrm{m}$. (a) $m = 0$ and (b) $m = 5$.

for the same $T_m(\rho_1, \rho_2, k_z)$, also with $m = 0$ and $m = 5$. Fixing $\rho_1 = 1.0\lambda$, the k_z spectrum is shown for ρ_2 ranging from 1.0λ to 0.9λ. Note that the maximum inward distance is only 0.1λ for this example. Much more radical high-pass filtering is found for larger distances. For example, had ρ_1 been 1.4λ the peak values at $\rho_2 = 0.9\lambda$ for the $m = 0$ case would be 1.5×10^8.

The outbound low-pass and inbound high-pass nature of the translation operators also appears in the azimuthal frequency index, m. Examples of this behavior are shown in Figure 5, where k_z-m spectra of $|T_m(\rho_1, \rho_2, k_z)|$, $|S1_m(\rho_1, \rho_2, k_z)|$ and $|S2_m(\rho_1, \rho_2, k_z)|$ are arrayed vertically in two columns. Outbound operators with $\rho_1 = 0.94$ m and $\rho_2 = 1.24$ m appear in the left column while the same operators appear in the right column for the inverse backpropagation case $\rho_1 = 1.24$ m and $\rho_2 = 0.94$ m. Operator magnitudes display mirror symmetry in both k_z and m. Self-term operators, T_m and $S1_m$, have even-symmetry. This is expected since change in the polarity of k_z or m merely indicates a reversal of modal propagation direction in z or ϕ on the cylinder surface. The cross-term operator, $S2_m$, has odd-symmetry in k_z and m, and is zero for $k_z = 0$ and for $m = 0$, as is apparent from (22c). With $m = 0$, $S1_m$ simplifies to the ratio $H_0^{(2)'}(k_\rho \rho_2)/H_0^{(2)}(k_\rho \rho_1)$.

Note that $S1_m$ and $S2_m$ in (22) share the same denominator. This term is proportional to the determinant of $[V_m(\rho_1, k_z)]$ and results from the array inverse appearing in (20c). At any specified ρ_1 the denominator of $S1_m$ and $S2_m$ will have local minima in k_z-m corresponding to reduced conditioning of the $[V_m]$ array. These minima change with ρ_1 and induce localized spikes in the transfer functions, as can be seen in the bottom two rows of Figure 5.

Backpropagation is accompanied by extreme high-pass filtering as depicted in the right column of Figure 5. Low-pass filtering is essential to compensate for the resultant amplification of noise and numerical errors. A simple single-parameter Wiener filter [13, 19] was used for short backpropagation distances ($< 0.1\lambda$) in the early phases of this research. Later, a linear 2-D low-pass filter was developed which offers improved performance over longer backpropagation distances. This filter provides unit transfer function over an elliptically shaped low-pass k_z-m region, with Gaussian roll-off beyond the boundary. Defining a normalized elliptical spectral radius,

$$R(k_z, m) = \sqrt{\left(\frac{k_z}{k_B}\right)^2 + \left(\frac{m}{m_B}\right)^2} \tag{23}$$

with bandwidths of k_B and m_B, the 2-D filter has the form,

$$Q_m(k_z) = 1 \qquad \text{for R} < 1 \tag{24a}$$

$$Q_m(k_z) = \exp\left\{-\frac{(R-1)^2}{2\sigma_R^2}\right\} \quad \text{for } R > 1 \tag{24b}$$

where σ_R is the normalized standard deviation for filter rolloff.

An example of $Q_m(k_z)$ is shown in Figure 6(a) for $\sigma_R = 0.2$ with $k_B = 36$ and $m_B = 16$. Multiplication of the high-pass $|T_m|$

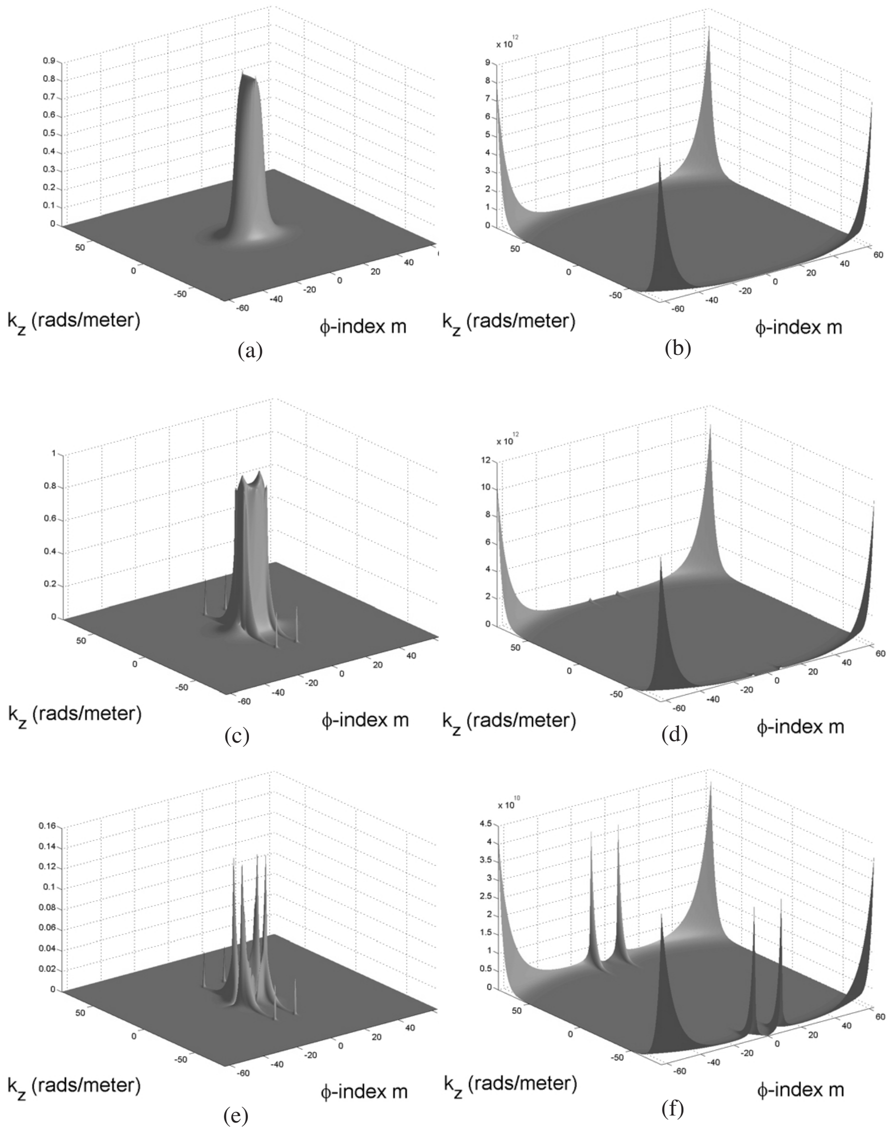

Figure 5. $|T_m(\rho_1, \rho_2, k_z)|$ for (a) Outward translation $\rho_1 = 0.94\,\mathrm{m} \rightarrow \rho_2 = 1.24\,\mathrm{m}$ and (b) Inward translation (backpropagation) $\rho_1 = 1.24\,\mathrm{m} \rightarrow \rho_2 = 0.94\,\mathrm{m}$; $|S1_m(\rho_1, \rho_2, k_z)|$ for (c) Outward translation $\rho_1 = 0.94\,\mathrm{m} \rightarrow \rho_2 = 1.24\,\mathrm{m}$ and (d) Inward Translation $\rho_1 = 1.24\,\mathrm{m} \rightarrow \rho_2 = 0.94\,\mathrm{m}$; $|S2_m(\rho_1, \rho_2, k_z)|$ for (e) Outward translation $\rho_1 = 0.94\,\mathrm{m} \rightarrow \rho_2 = 1.24\,\mathrm{m}$ and (f) Inward translation $\rho_1 = 1.24\,\mathrm{m} \rightarrow \rho_2 = 0.94\,\mathrm{m}$.

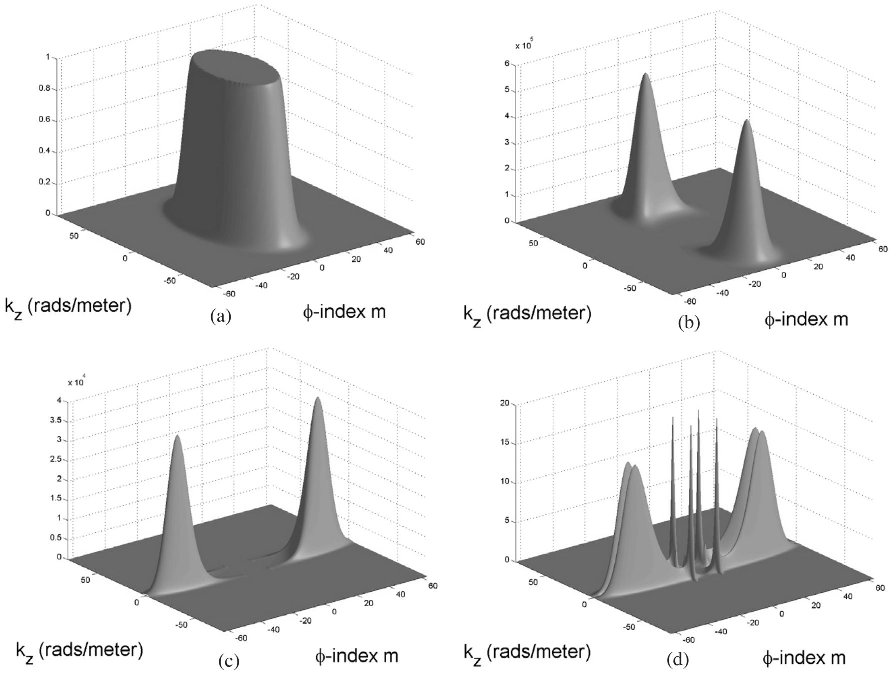

Figure 6. (a) Example $|Q_m(k_z)|$ for backpropagation: $\rho_1 = 1.24\,\mathrm{m} \rightarrow \rho_2 = 0.94\,\mathrm{m}$; (b) $|Q_m(k_z)\ T_m(\rho_1, \rho_2, k_z)|$; (c) $|Q_m(k_z)\ S1_m(\rho_1, \rho_2, k_z)|$; (d) $|Q_m(k_z)\ S2_m(\rho_1, \rho_2, k_z)|$.

shown in Figure 5(b) gives the filtered operator in Figure 6(b) for backpropagation from $\rho_1 = 1.24\,\mathrm{m}$ to $\rho_2 = 0.94\,\mathrm{m}$. Multiplying the corresponding high-pass $|S1_m|$ and $|S1_m|$ in Figure 5 by $Q_m(k_z)$ (also having $\sigma_R = 0.2$ but with $k_B = 8$ and $m_B = 32$) gives the filtered $|Q_m\ S1_m|$ and $|Q_m\ S2_m|$ in Figures 6(c-d).

5. PERFORMANCE TESTS

Extensive tests were performed for outward and inward radial translation of both noise-free and additive noise fields at $f = 300\,\mathrm{MHz}$ generated by the previously described three-element N P S wire array. This array is conformal to a cylinder of radius $\rho = 0.90\,\mathrm{m}$, as shown in Figure 1. Tangential field components were computed at grid points on 24 geometric cylinders, each of length 20 m and with $\rho = 0.94\,\mathrm{m}$, $0.96\,\mathrm{m}, \ldots, 1.38\,\mathrm{m}, 1.40\,\mathrm{m}$. The cylindrical grid has 512 equispaced points in z and 128 equispaced points in ϕ, a total of 65,536 points on each cylinder. Source segmentation was increased until computed fields converged to at least four decimal places at all grid points. These reference fields will be referred to as "exact" in the discussion to follow.

Complex noise having independent Gaussian densities for real and imaginary parts was added to the exact field components at the grid points on the various cylinders to give signal-to-noise ratios (SNR) of 40 dB, 30 dB and 20 dB. The SNR is computed using ratios of sums of squared magnitudes for exact field phasors at the grid points to those of complex noise that is being added. For example, SNR for the E_z field is

$$E_z\ \text{SNR} = 10\ \log_{10}\left[\frac{\sum\limits_{\text{All }(\phi,z)} |\text{Exact } E_z|^2}{\sum\limits_{\text{All }(\phi,z)} |\text{Noise } N_z|^2}\right]\ (\text{dB}) \tag{25}$$

The first test series to be considered involves outward translation of $\overline{E}_{tan} = E_z\hat{z}+E_\phi\hat{\phi}$ and $\overline{H}_{tan} = H_z\hat{z}+H_\phi\hat{\phi}$ with and without additive noise on the $\rho_1 = 0.94$ m cylinder. Translation is made to the remaining 23 conformal cylinders with RMS error evaluated by comparison with the exact fields at the cylinder surface grid points. For instance,

$$\overline{E}_{tan}\ \text{RMS Error} = 100\ \%\sqrt{\frac{\sum\limits_{\text{All }(\phi,z)} |(\text{Exact } \overline{E}_{tan}) - (\text{Translated } \overline{E}_{tan})|^2}{\sum\limits_{\text{All }(\phi,z)} |\text{Exact } \overline{E}_{tan}|^2}} \tag{26}$$

The left column of Figure 7 depicts log-intensity magnitudes of tangential field components for the worst-case 20 dB SNR on the unwrapped cylinder at $\rho_1 = 0.94$ m with spatial coordinates $\rho\phi$ and z. Corresponding k_z-m log-intensity spectral magnitudes appear in the right column. The H-field components in the left column have a higher spatial resolution than the E-field, with intensities proportional to $\hat{\rho}\times\overline{I}$ of the nearby N P S current segments. This higher resolution generates the wider spectral bandwidth of the H-field shown in the right column plots.

Outward translation of these noisy fields to $\rho_2 = 1.24$ m without filtering by $Q_m(k_z)$ gives the tangential field magnitudes in the right column of Figure 8, with comparison to the exact fields in the left column. RMS error for $\overline{E}_{tan}$ is about 6.6% while that for $\overline{H}_{tan}$ is about 4.7%. Apparent errors are amplified by the log-intensity of the

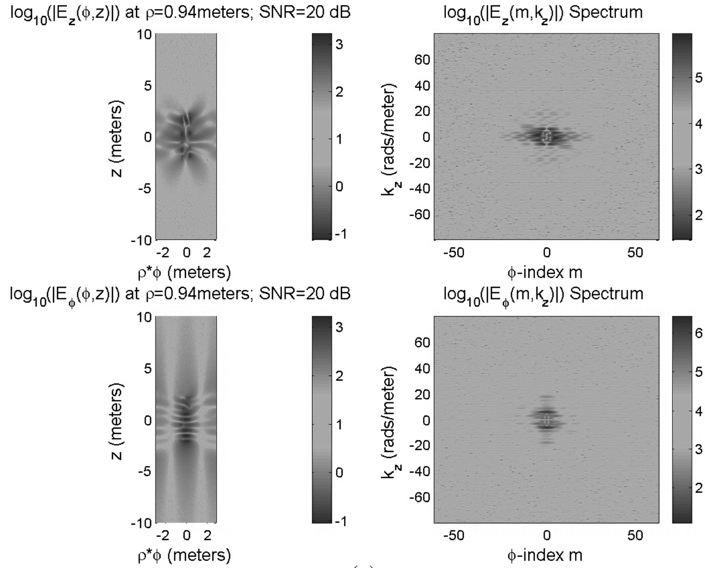

(a)

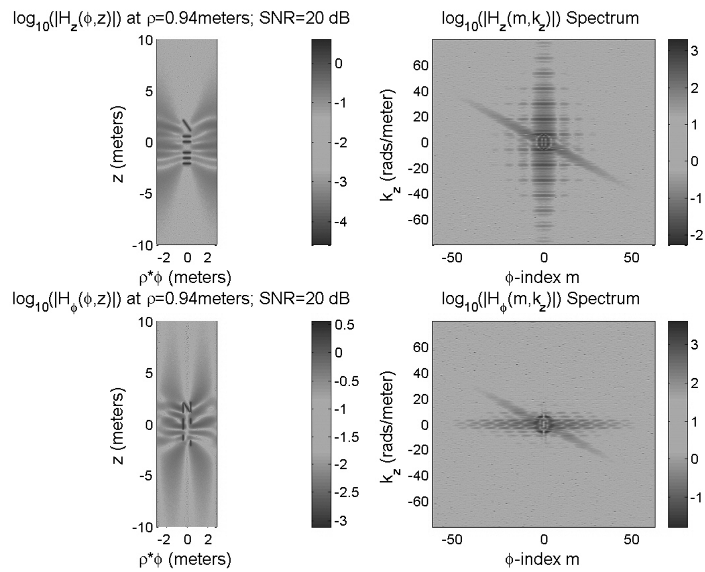

(b)

Figure 7. Tangential field components with additive noise (SNR $= 20\,\text{dB}$) on $\rho_1 = 0.94\,\text{m}$ cylinder with associated 2-D spectra. (a) $\log_{10}\{|E_z(\rho_1,\phi,z)|\}$, $\log_{10}\{|\mathcal{E}_{z,m}(\rho_1,k_z)|\}$, $\log_{10}\{|E_\phi(\rho_1,\phi,z)|\}$, and $\log_{10}\{|\mathcal{E}_{\phi,m}(\rho_1,k_z)|\}$; (b) $\log_{10}\{|H_z(\rho_1,\phi,z)|\}$, $\log_{10}\{|\mathcal{H}_{z,m}(\rho_1,k_z)|\}$, $\log_{10}\{|H_\phi(\rho_1,\phi,z)|\}$, and $\log_{10}\{|\mathcal{H}_{\phi,m}(\rho_1,k_z)|\}$.

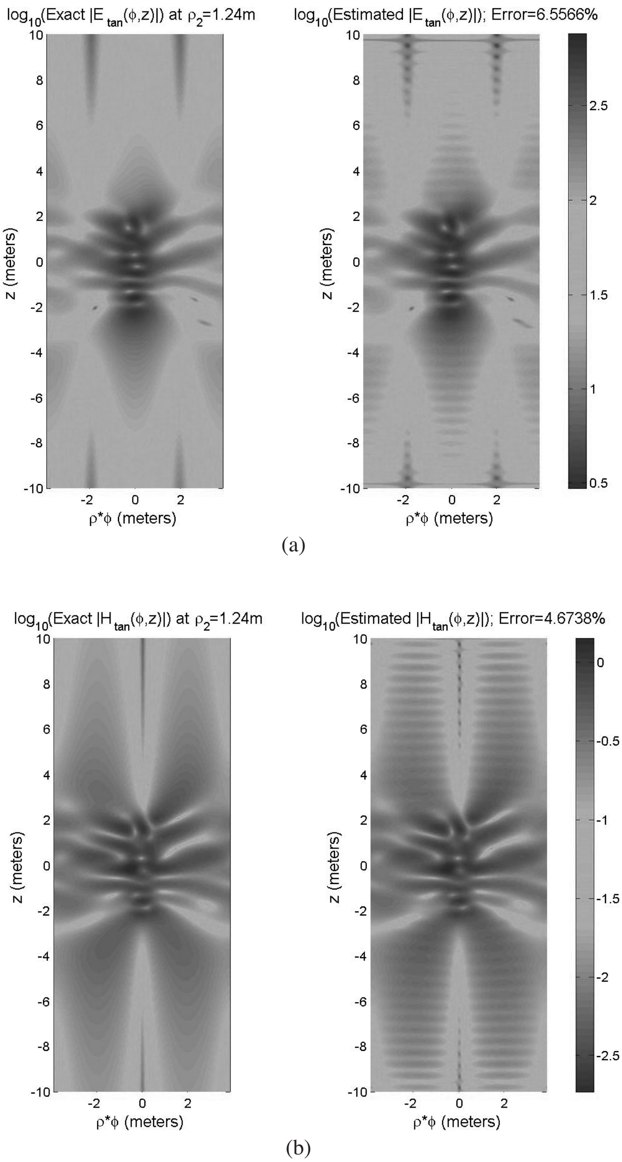

Figure 8. Comparing exact and computed tangential field components on $\rho_2 = 1.24\,\mathrm{m}$ cylinder translated $\Delta\rho = 0.3\lambda$ from $\rho_1 = 0.94\,\mathrm{m}$ using data with SNR $= 20\,\mathrm{dB}$: (a) $\log_{10}\{|\overline{E}_{tan}(\rho_2, \phi, z)|\}$; (b) $\log_{10}\{|\overline{H}_{tan}(\rho_2, \phi, z)|\}$.

plots in regions most distant from the source where the tangential fields are smallest. This appears most strongly in ripples nearest to the cylinder ends caused by interference of fields produced by the real truncated source cylinder at ρ_1 and the adjacent virtual replicas of this truncated cylinder. These virtual source replicas form part of an infinite periodic array in z that results from use of the Fourier series (and associated FFT) in lieu of the continuous k_z transform for the infinite length cylinder.

Summary of RMS errors in $\overline{E}_{tan}$ and $\overline{H}_{tan}$ for outward translation cases from $\rho_1 = 0.94\,\mathrm{m}$ is shown in Figure 9. Notice that for ρ_2 greater than about $1\,\mathrm{m}$ (distances $> 0.1\ \lambda$ from the source) errors increase almost linearly with distance and are nearly equal for the four levels of additive noise. The noise insensitivity results from the extensive low-pass filtering being performed by the outbound translation operators. Increase of error with increasing ρ_2 is caused by progressively larger regions of interference from the adjacent virtual replicas of the ρ_1 source cylinder. Field contributions at a point on the ρ_2 cylinder are generated by tangential fields on the ρ_1 cylinder with contributions weighted by powers of inverse electrical distance: $(\lambda/R)^n$ with $n = 1, 2$ for $\overline{E}$ and $\overline{H}$ and $n = 3$ for $\overline{E}$. If ρ_2 is electrically close to ρ_1, source contributions are strongly weighted in the closest small patch region on the ρ_1 cylinder. Points near to the ends of the truncated ρ_2 cylinder will suffer the largest relative error from this effect since more of their strongly weighted source contributions are supplied by the adjacent virtual source cylinder. The region being affected near to the ends increases in size as ρ_2 grows. At the other extreme, as $\rho_2 \to \rho_1$ the error increases and becomes sensitive to SNR. This is due to FFT aliasing for the spatial sampling used on the cylindrical grid. Errors shown include use of $Q_m(k_z)$ filtering to reduce error for the 30 dB and 20 dB additive noise cases when $\rho_2 < 1.1\,\mathrm{m}$. Otherwise, no filtering was used in these outward translation tests.

Backpropagation was investigated for fixed $\rho_2 = 0.94\,\mathrm{m}$ and 23 values of ρ_1, ranging from $0.96\,\mathrm{m}$ to $1.40\,\mathrm{m}$ with the four levels of additive noise. For example, field component magnitudes with 20 dB SNR are arrayed on the left of Figure 10 for the $\rho_1 = 1.04\,\mathrm{m}$ cylinder, with associated spectra on the right. These narrow spectra are to be translated just 0.1λ back to the $\rho_4 = 0.94\,\mathrm{m}$ cylinder, whose fields have the much wider spectra shown in Figure 7. The operators in (19) and (22) accomplish this high-pass filtering task in the theoretical sense but require practical augmentation by low-pass filtering for even electrically small backpropagation distances. Quasi-optimal elliptical filters, $Q_m(k_z)$, were found in each case by rough search on the bandwidth parameters k_B and m_B (with increments of 4). One set

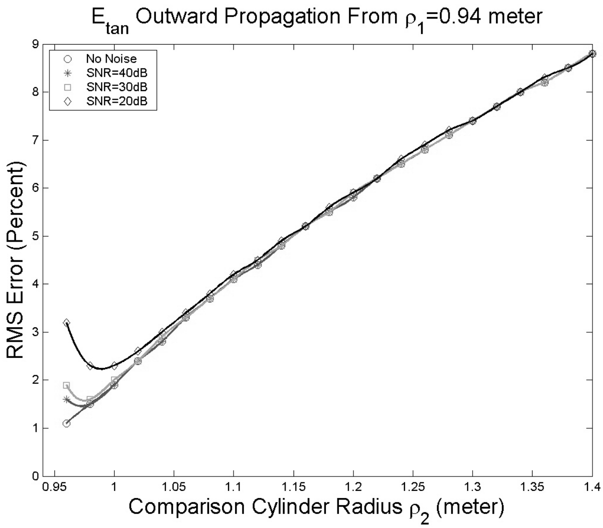

(a)

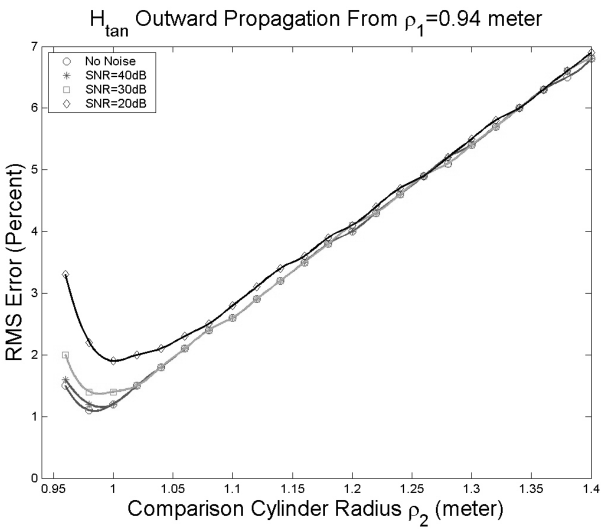

(b)

Figure 9. Tangential field RMS errors on ρ_2 for outward translation from $\rho_1 = 0.94\,\mathrm{m}$ using data with specified SNR: (a) Errors in $\overline{E}_{tan}(\rho_2, \phi, z)$; (b) Errors in $\overline{H}_{tan}(\rho_2, \phi, z)$.

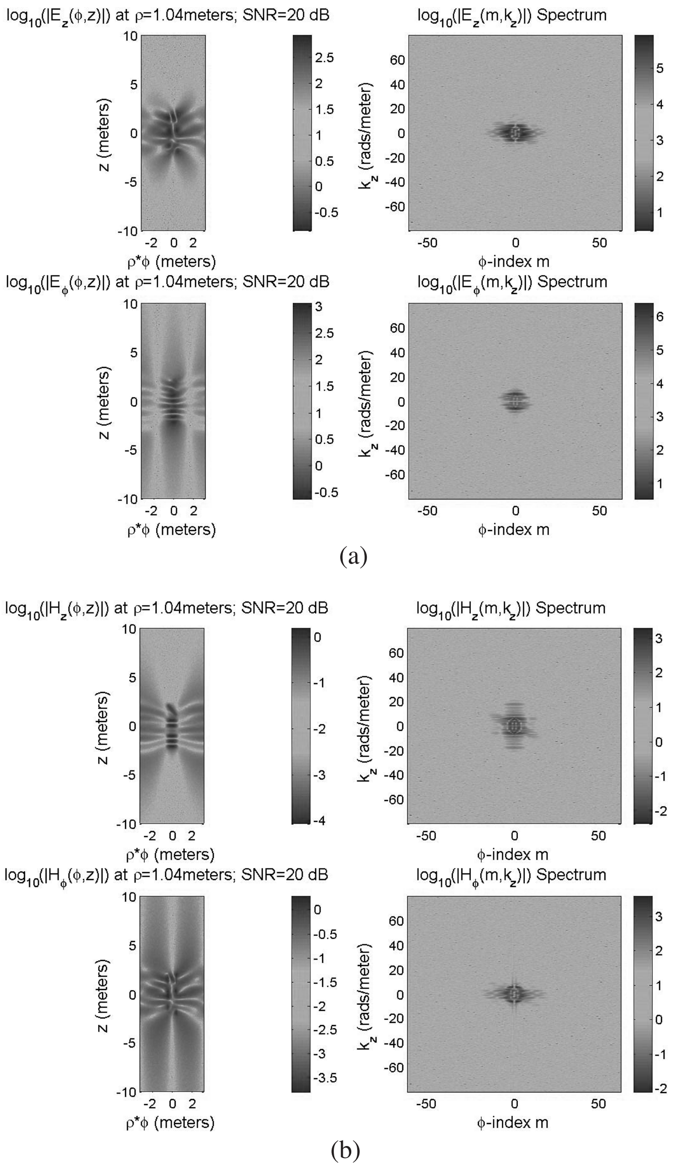

Figure 10. Tangential field components with additive noise (SNR $= 20\,\mathrm{dB}$) on $\rho_1 = 1.04\,\mathrm{m}$ cylinder with associated 2-D spectra. (a) $\log_{10}\{|E_z(\rho_1,\phi,z)|\}$, $\log_{10}\{|\mathcal{E}_{z,m}(\rho_1,k_z)|\}$, $\log_{10}\{|E_\phi(\rho_1,\phi,z)|\}$, and $\log_{10}\{|\mathcal{E}_{\phi,m}(\rho_1,k_z)|\}$; (b) $\log_{10}\{|H_z(\rho_1,\phi,z)|\}$, $\log_{10}\{|\mathcal{H}_{z,m}(\rho_1,k_z)|\}$, $\log_{10}\{|H_\phi(\rho_1,\phi,z)|\}$, and $\log_{10}\{|\mathcal{H}_{\phi,m}(\rho_1,k_z)|\}$.

of parameters was used with the filter to compensate T_m (translating both E_z and H_z) while another set was used to define a common filter for $S1_m$ and $S2_m$ to translate E_ϕ and H_ϕ. Using only two different filters for each case, with step increments of 4 in searches over the k_B-m_B space, reduced the iteration time for all cases to about 12 hours on a 2 GHz Pentium-4 computer.

Figure 11 compares exact fields on the $\rho_2 = 0.94\,\mathrm{m}$ cylinder to those backpropagated from noiseless fields on $\rho_1 = 1.04\,\mathrm{m}$. Errors for $\overline{E}_{tan}$ and $\overline{H}_{tan}$ are 9.7% and 12.5%, respectively using filter parameters $k_B = 72$, $m_B = 48$ for E_z-H_z and $k_B = 40$, $m_B = 64$ for E_ϕ-H_ϕ. Comparisons are shown in Figure 12 for the same cylinder but for backpropagation of noisy fields with SNR = 20 dB at $\rho_1 = 1.04\,\mathrm{m}$. Intensity scales are slightly different from those of Figure 11 due to automatic settings that accommodate the full dynamic range in the pairs of field components being compared. Errors for this worst case SNR are about 17.5% for $\overline{E}_{tan}$ and 26.5% for $\overline{H}_{tan}$ using $k_B = 24$, $m_B = 16$ for E_z-H_z and $k_B = 16$, $m_B = 20$ for E_ϕ-H_ϕ. Generally, the filter bandwidth parameters k_B and m_B are reduced both for increased backpropagation distance and for lower SNR.

Increasing ρ_1 to 1.24 m (0.34λ from the source cylinder) the tangential fields with SNR = 20 dB are shown in Figure 13. Note the collapsed bandwidth with only faint energy outside of the radiation region $|k_z| < k_0 = 2\pi$ (for $f = 300\,\mathrm{MHz}$). Again, the task of the translation operators is to resurrect the broad spectral content of the fields at $\rho_2 = 0.94\,\mathrm{m}$ as depicted in Figure 7. Figure 14 shows the result for the noise-free case, with $\overline{E}_{tan}$ and $\overline{H}_{tan}$ errors of 18.7% and 17.9% using $k_B = 36$, $m_B = 16$ for E_z-H_z and $k_B = 8$, $m_B = 32$ for E_ϕ-H_ϕ. Fields comparison for the corresponding 20 dB case is displayed in Figure 15. Errors are 20.9% for $\overline{E}_{tan}$ and 45.8% for $\overline{H}_{tan}$ with $k_B = 8$, $m_B = 12$ used for E_z-H_z backpropagation and $k_B = 8$, $m_B = 8$ used for E_ϕ-H_ϕ.

RMS errors in backpropagation from all 23 values of ρ_1 for the various noise levels are summarized in Figure 16. As expected, errors generally increase with both larger ρ_1 and lower SNR. Further, $\overline{H}_{tan}$ usually suffers larger error than does $\overline{E}_{tan}$ since the high resolution of $\overline{H}_{tan}$ at $\rho_2 = 0.94\,\mathrm{m}$ (see Figure 7) has a wide bandwidth which is difficult to accurately construct using the filtered backpropagation process.

It should be noted that these results are obtained by compensating the high-pass T_m for both E_z and H_z using a common $Q_m(k_z)$ that minimizes the sum of their RMS errors. This quasi-optimal filter is found through search over k_B-m_B space using a step size of four for each parameter. A common $Q_m(k_z)$ is also used to compensate both

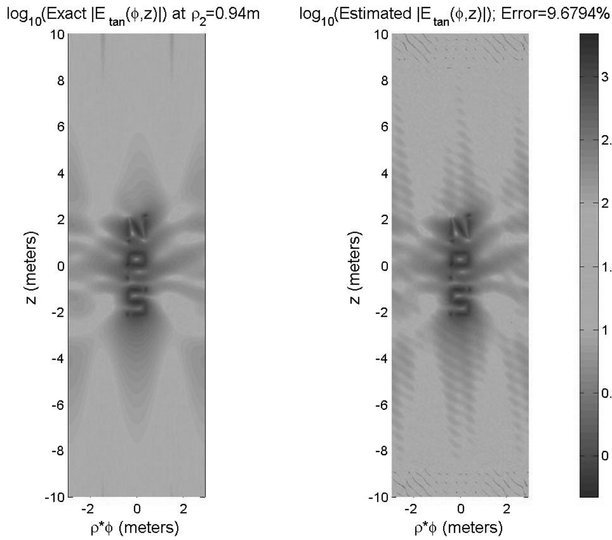

(a)

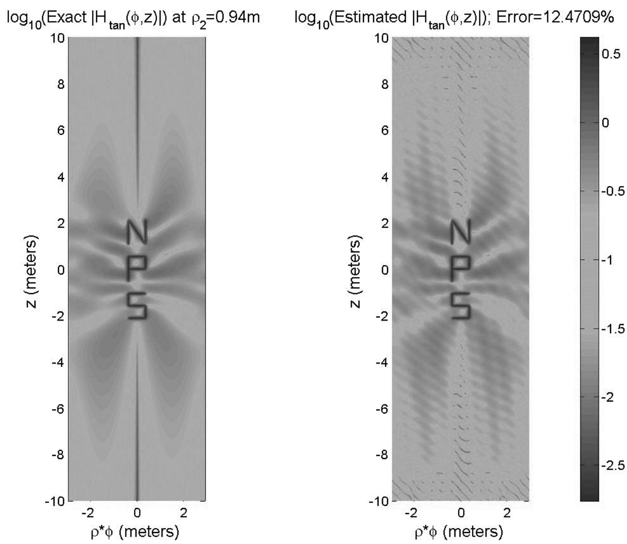

(b)

Figure 11. Comparing exact and computed tangential field components on $\rho_2 = 0.94\,\mathrm{m}$ cylinder backpropagated $\Delta\rho = \lambda/10$ from $\rho_1 = 1.04\,\mathrm{m}$ using noise-free data: (a) $\log_{10}\{|\overline{E}_{tan}(\rho_2, \phi, z)|\}$; (b) $\log_{10}\{|\overline{H}_{tan}(\rho_2, \phi, z)|\}$.

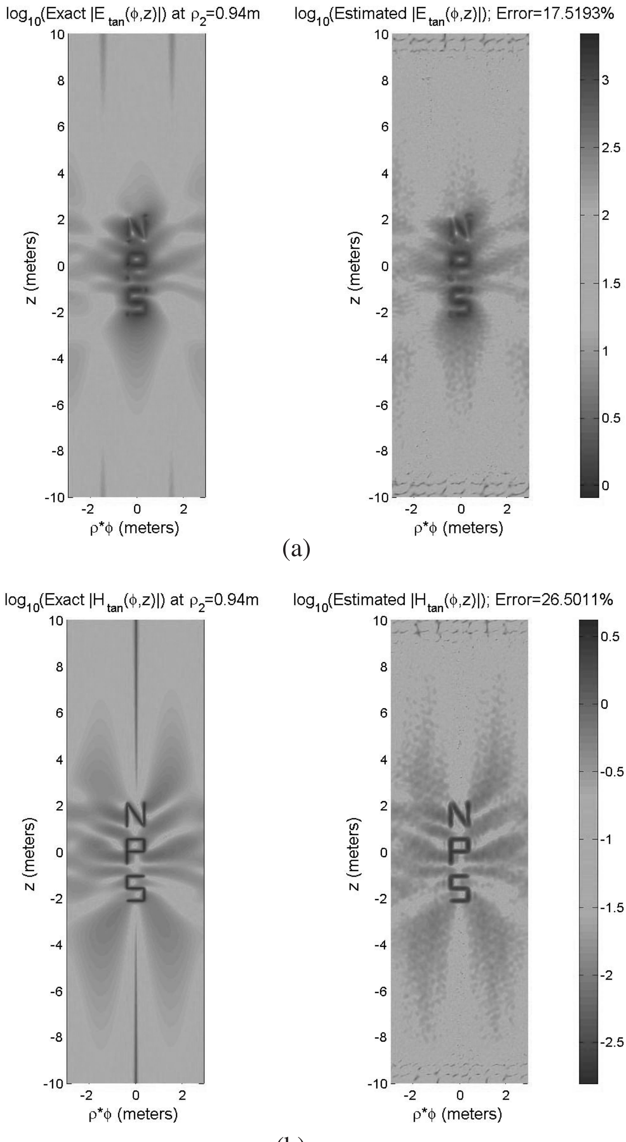

Figure 12. Comparing exact and computed tangential field components on $\rho_2 = 0.94\,\mathrm{m}$ cylinder backpropagated $\Delta\rho = \lambda/10$ from $\rho_1 = 1.04\,\mathrm{m}$ using data with SNR $= 20\,\mathrm{dB}$: (a) $\log_{10}\{|\overline{E}_{tan}(\rho_2, \phi, z)|\}$; (b) $\log_{10}\{|\overline{H}_{tan}(\rho_2, \phi, z)|\}$.

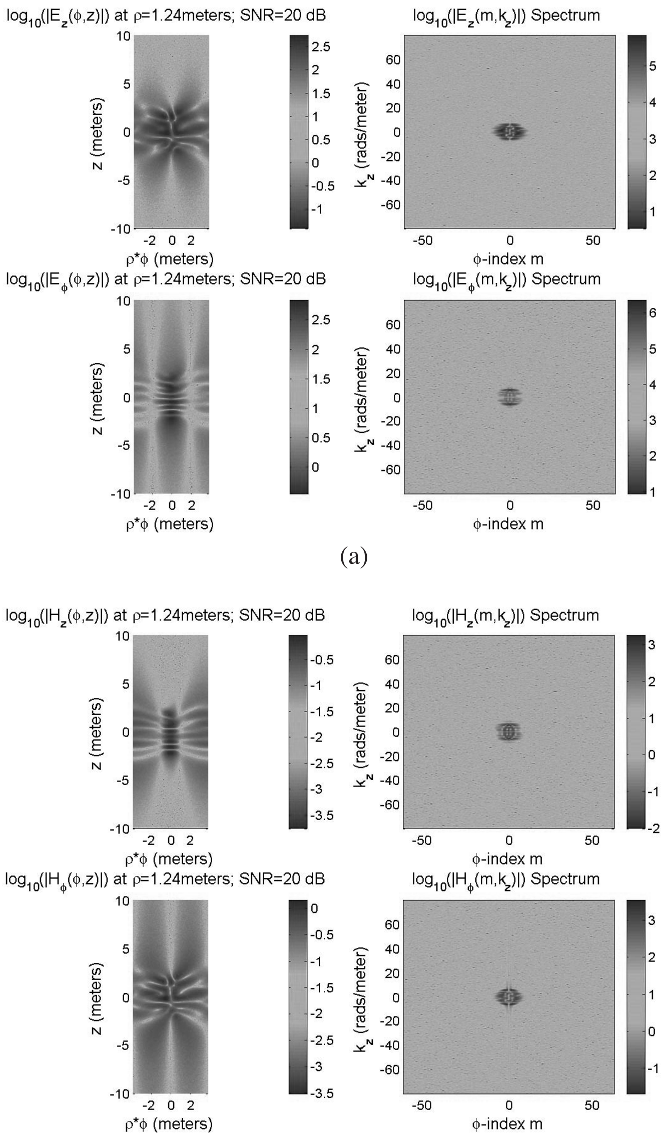

(a)

(b)

Figure 13. Tangential field components with additive noise (SNR $= 20\,\mathrm{dB}$) on $\rho_1 = 1.24\,\mathrm{m}$ cylinder with associated 2-D spectra. (a) $\log_{10}\{|E_z(\rho_1,\phi,z)|\}$, $\log_{10}\{|\mathcal{E}_{z,m}(\rho_1,k_z)|\}$, $\log_{10}\{|E_\phi(\rho_1,\phi,z)|\}$, and $\log_{10}\{|\mathcal{E}_{\phi,m}(\rho_1,k_z)|\}$; (b) $\log_{10}\{|H_z(\rho_1,\phi,z)|\}$, $\log_{10}\{|\mathcal{H}_{z,m}(\rho_1,k_z)|\}$, $\log_{10}\{|H_\phi(\rho_1,\phi,z)|\}$, and $\log_{10}\{|\mathcal{H}_{\phi,m}(\rho_1,k_z)|\}$.

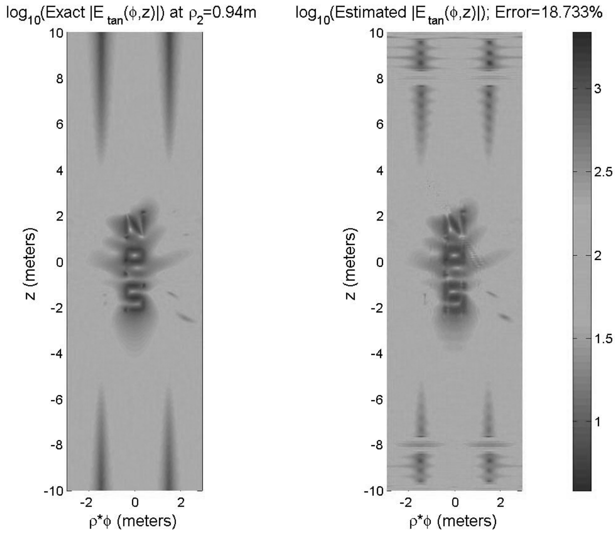

(a)

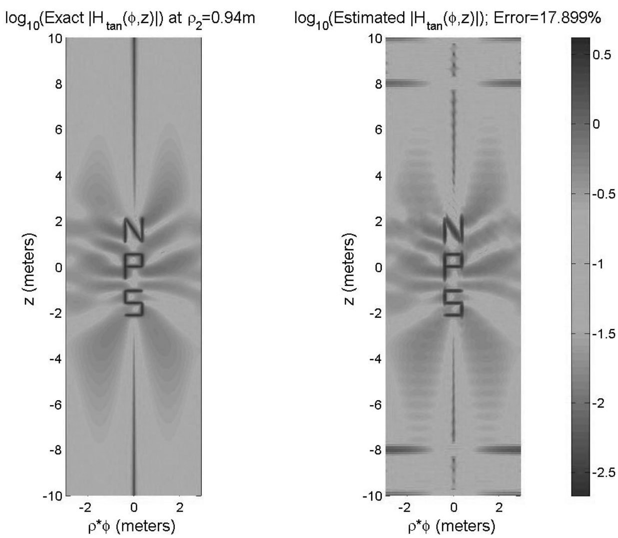

(b)

Figure 14. Comparing exact and computed tangential field components on $\rho_2 = 0.94\,\mathrm{m}$ cylinder backpropagated $\Delta\rho = 0.3\lambda$ from $\rho_1 = 1.04\,\mathrm{m}$ using noise-free data: (a) $\log_{10}\{|\overline{E}_{tan}(\rho_2, \phi, z)|\}$; (b) $\log_{10}\{|\overline{H}_{tan}(\rho_2, \phi, z)|\}$.

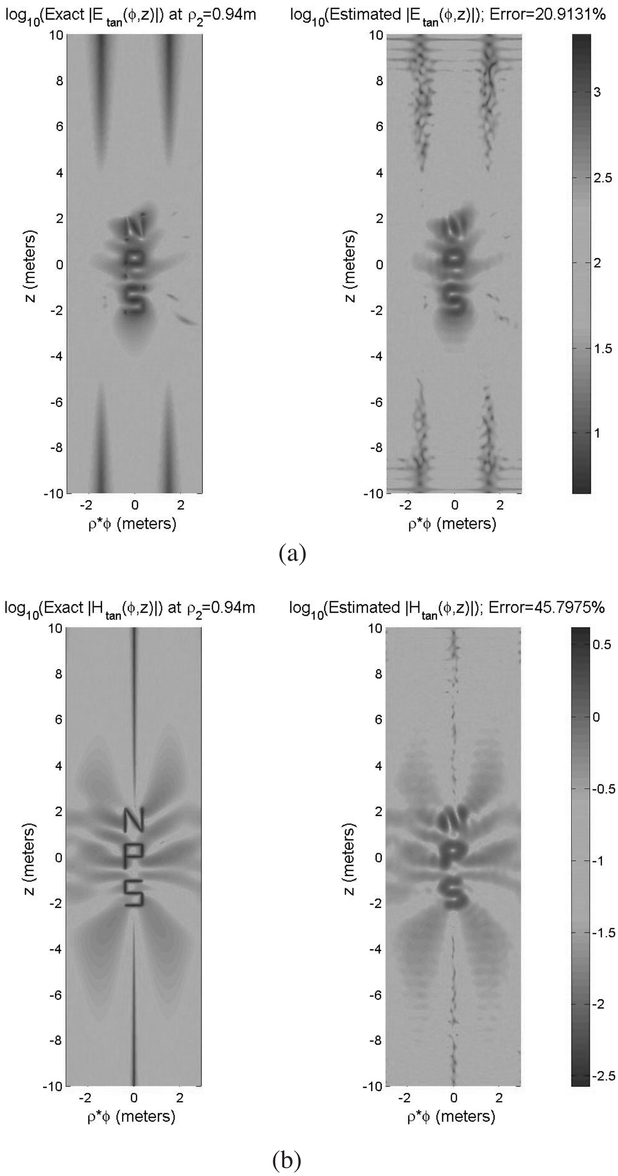

Figure 15. Comparing exact and computed tangential field components on $\rho_2 = 0.94\,\mathrm{m}$ cylinder backpropagated $\Delta\rho = 0.3\lambda$ from $\rho_1 = 1.04\,\mathrm{m}$ using data with SNR $= 20\,\mathrm{dB}$: (a) $\log_{10}\{|\overline{E}_{tan}(\rho_2, \phi, z)|\}$; (b) $\log_{10}\{|\overline{H}_{tan}(\rho_2, \phi, z)|\}$.

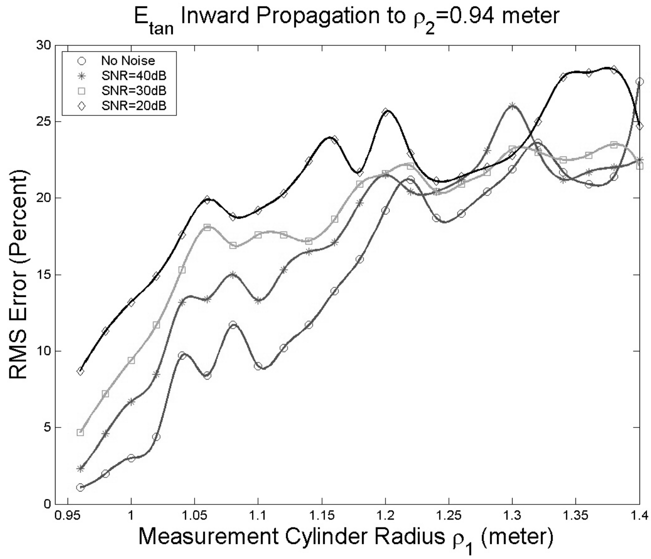

(a)

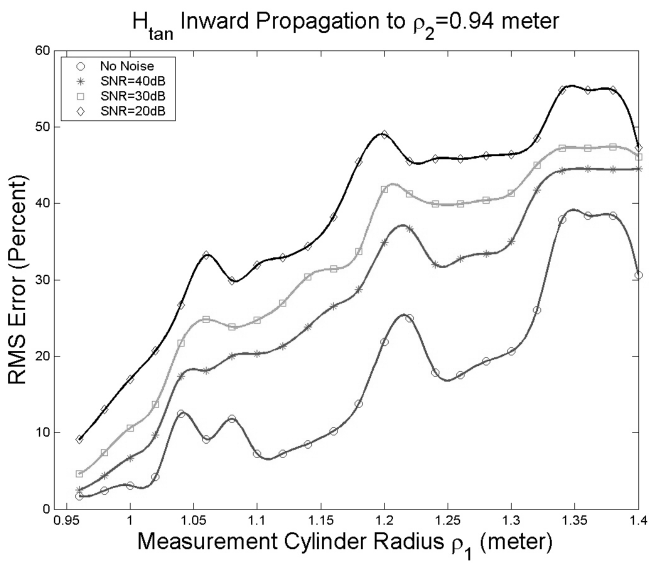

(b)

Figure 16. Tangential field RMS errors on $\rho_2 = 0.94\,\mathrm{m}$ for backpropagation using data with specified SNR on $\rho_1 > \rho_2$: (a) Errors in $\overline{E}_{tan}(\rho_2, \phi, z)$; (b) Errors in $\overline{H}_{tan}(\rho_2, \phi, z)$.

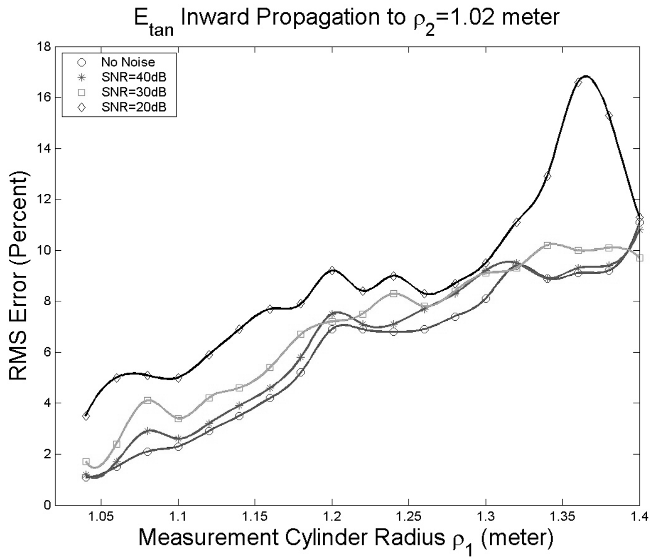

(a)

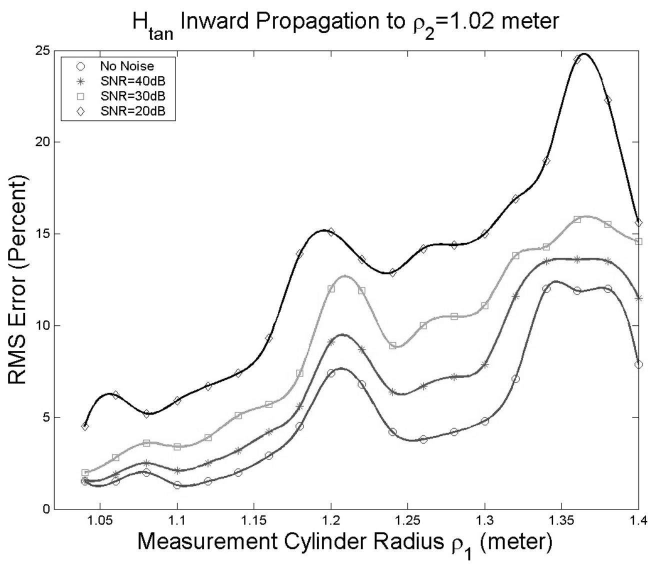

(b)

Figure 17. Tangential field RMS errors on $\rho_2 = 1.04\,\mathrm{m}$ for backpropagation using data with specified SNR on $\rho_1 > \rho_2$: (a) Errors in $\overline{E}_{tan}(\rho_2, \phi, z)$; (b) Errors in $\overline{H}_{tan}(\rho_2, \phi, z)$.

$S1_m$ and $S2_m$ by seeking to minimize the sum of errors for E_ϕ and H_ϕ with the same large-step k_B-m_B search procedure.

Another set of tests was performed by backpropagating to $\rho_2 = 1.04\,\mathrm{m}$ using tangential fields on the 19 larger cylinders. A summary of RMS errors is shown in Figure 17. Errors here show the expected increase with larger ρ_1 and with lower SNR but are all somewhat lower than those found in Figure 16, especially for $\overline{H}_{tan}$. The reason for this improvement is the less demanding spectral conversion being attempted for this larger target radius. This can be seen by comparing the spectra for $\rho_2 = 0.94\,\mathrm{m}$ in Figure 7 to those for $\rho_2 = 1.04\,\mathrm{m}$ in Figure 10. At $\rho_2 = 1.04\,\mathrm{m}$ the spectral widths of $\overline{E}_{tan}$ and $\overline{H}_{tan}$ are both narrower and more comparable than at $\rho_2 = 0.94\,\mathrm{m}$.

6. CONCLUSIONS

A theoretical formulation for field translation between concentric cylindrical surfaces has been derived using spectral decomposition in k_z-m space. The theory is applied to spatially sampled fields on finite cylinders with various noise levels and tested extensively for a specific source example. The translation procedure forms the basis for microwave holography by backpropagating fields measured on a finite cylinder of radius ρ_1 onto cylinders having radii $\rho_2 < \rho_1$ that more tightly enclose the source.

As shown, time-average radiated power is exclusively generated by superluminal modes ($v_z > c$) with $|k_z| < k_0$. Subluminal modes, with $|k_z| > k_0$, provide essential resolution beyond the diffraction limited radiation. These high-resolution modes are, however, radially evanescent and decay rapidly with distance from the source. This evanescence is manifested by low-pass filtering of subluminal spectral components in both k_z and m that accompanies outward translation of fields.

Backpropagation is demonstrated to involve a high-pass filtering process which greatly amplifies noise or measurement error. Compensation by adjustable low-pass filtering is essential to mitigate this noise amplification. A 2-D filter with unit value elliptical passband and Gaussian roll-off was used to provide this required compensation. Quasi-optimal filters for each tested case were found by a search in a k_z-m parameter space using RMS error sums for field component pairs (E_z, H_z) and (E_ϕ, H_ϕ) as cost functions.

Example tests involve spatially sampled fields from a cylindrically conformal wire array source with four levels of additive noise ranging from noise-free to 20 dB SNR. These tests consider both outward and inward translation. Outward translation provides innate low-pass filtering. Errors for outward translations beyond about 0.1λ from the source are caused primarily by the use of truncated cylinders. This error increases almost linearly with translation distance for the example cases. For translation distances less than 0.1λ, limitations on spatial sampling produces aliasing of broadband noise. Moderate low-pass filtering is employed to reduce this error for the two lowest SNR cases.

Backpropagation tests were conducted for two ρ_2 target radii. As expected, errors generally increase with larger ρ_1 radius and with reduced SNR. Errors were also somewhat larger for the noisy H-field cases compared to those for the E-field when backpropagating to the smaller ρ_2. This resulted from the need to create a very wide 2-D spectrum that was observed for the H-field so close to the wire source. Accuracy was improved for backpropagation to the larger ρ_2 since the spectral widths of the target fields were much narrower and thus less demanding on the reconstruction process. The spectral widths were also more similar for the E-field and H-field which resulted in more comparable errors.

As noted, the backpropagation filtering employed in the tests was not fully optimized. Even with these limitations the results of this initial effort demonstrate backpropagation of relatively noisy fields from distances as great as 0.46λ to create enhanced resolution images on cylinder surfaces much closer to the source. Improvement in accuracy and the extension of useful backpropagation distance can be expected with further refinements such as non-uniform spatial sampling, systematic cylinder truncation, and perhaps the creation of self-adaptive application-specific 2-D filters.

ACKNOWLEDGMENT

The author gratefully acknowledges support for this work by the Office of Naval Research, Code 334, Ship Hull, Mechanical and Electrical Systems Science and Technology Division.

REFERENCES

1. Ransom, P. L. and R. Mittra, "A method of locating defective elements in large phased arrays," *Proc. IEEE*, Vol. 59, 1029–1030, 1971.
2. Harms, P. H., J. G. Maloney, M. P. Kesler, E. J. Kunster, and G. S. Smith, "A system for unobtrusive measurement of surface currents," *IEEE Trans. Antennas Propagat.*, Vol. 49, 174–185, 2001.

3. Guler, M. G. and E. B. Joy, "High resolution spherical microwave holography," *IEEE Trans. Antennas Propagat.*, Vol. 43, 464–472, 1995.
4. Joy, E. B., M. G. Guler, C. H. Barrett, A. R. Dominy, and R. E. Wilson, "Near-field measurement of radome anomalies," *Proc. 9th Antenna Measurement Tech. Assoc. Symposium*, 235–240, October 1987.
5. Guler, M. G., "Spherical microwave holography," Ph.D. dissertation, Georgia Tech., Atlanta, GA, Dec. 1993.
6. Medgyesi-Mitchang, L. N., P. G. Moore, D. L. Smith, and S. G. Lambrakos, "Ultra-near fields of bodies of translation with discontinuities: $\omega - k$ representations," *J. Electromagn. Waves Appl.*, Vol. 15, 1701–1723, 2001.
7. Medgyesi-Mitchang, L. N., P. G. Moore, D. L. Smith, and S. G. Lambrakos, "Ultra-near fields of penetrable bodies of translation: $\omega - k$ representations," *J. Electromagn. Waves Appl.*, Vol. 16, 1467–1483, 2002.
8. Wawrzyniak, D. J., "Electromagnetic imaging of electromagnetic scatterers," M.S. thesis, Naval Postgraduate School, Monterey, CA, June 1997.
9. Williams, E. G., *Fourier Acoustics: Sound Radiation and Nearfield Acoustical Holography*, Academic Press, 1999.
10. Williams, E. G., "Supersonic acoustic intensity," *J. Acoust. Soc. Am.*, Vol. 97, 121–127, 1995.
11. Williams, E. G., B. Houston, and J. A. Bucaro, "Experimental investigation of the wave propagation on a point-driven, submerged capped cylinder using k-space analysis," *J. Acoust. Soc. Am.*, Vol. 87, 513–522, 1990.
12. Williams, E. G., H. D. Dardy, and K. B. Washburn, "Generalized nearfield acoustical holography for cylindrical geometry: Theory and experiment," *J. Acoust. Soc. Am.*, Vol. 81, 389–407, 1987.
13. Morgan, M. A., "Electromagnetic source imaging using superluminal cylindrical modes," *Abstracts for USNC/URSI Radio Science Meeting*, 354, July 1999.
14. Morgan, M. A., "Near-field imaging using cylindrical harmonic backpropagation," *Abstracts for Progress in Electromagnetics Research Symposium*, 556, July 2000.
15. Stutzman, W. L. and G. A. Thiele, *Antenna Theory and Design*, 2nd Ed., Section 1.6, John Wiley and Sons, 1998.
16. Silver, S., *Microwave Antenna Theory and Design*, Chapter 7, McGraw-Hill, New York, 1949.

17. Ramo, S., J. R. Whinnery, and T. Van Duzer, *Fields and Waves in Communications Electronics*, 3rd Ed., Chapter 8, Wiley, New York, 1994.
18. Abramowitz, M. and I. A. Stegun, *Handbook of Mathematical Functions*, Chapter 9, Dover, New York, 1970.
19. Papoulis, A., *Signal Analysis*, Chapter 3, McGraw-Hill, New York, 1977.